

# Aluminum Steam Oxidation in the Framework of Long-Term Energy Storage: Experimental Analysis of the Reaction Parameters Effect on Metal Conversion Rate

Linda Barelli, Lorenzo Trombetti, Alessandro Di Michele, Luca Gammaitoni, Jakob Asenbauer, and Stefano Passerini\*

Aluminum is a promising material as an alternative green energy carrier thanks to its very high volumetric energy density and full recyclability. Aluminum oxidation with steam in the temperature range of 600–900 °C is investigated as an innovative and promising methodology for aluminum conversion resulting in hydrogen and heat production. Reaction times, hydrogen production rate and yield are assessed varying operational parameters such as temperature, steam to aluminum ratio, and gas hourly space velocity within the reactor. The conversion yield of aluminum is assessed at 73.13% at 900 °C and ambient pressure, with reaction times comparable with the one reported in the literature for water oxidation in batch-pressurized reactors. Moreover, over 750 °C, alumina is produced in microparticles, allowing reactor operating times up to 1 h without incurring in the clogging effect. The obtained results are promising for the continuous operating condition of a future full-scale reactor.

stated by the Annual Energy Outlook of 2021 (AEO 2021) of the International Energy Agency (IEA), which provides a detailed analysis on the current situation of the energy sector. The 2021 economic rebound was characterized by an increase in energy-related CO<sub>2</sub> emissions of about 1.5 Gt, reaching a total of 33 Gt worldwide and erasing two-thirds of the pandemic-related reduction seen in 2020. This increment highlights how the most part of the world energy supply is still represented by fossil fuels (79%). Even in the power generation sector, the one with the greatest share of renewable sources, more than 60% of the power generated still comes from fossil fuels.

Moreover, it depicts the future scenario that could unfold on the enacted measures to tackle climate change. According to the

scenario based on the pledges and National Determined Contributions (NDCs) made by the governments under the Paris agreement, the AEO 2021 assesses an expected rise in global mean temperature of 2.1 °C by 2100 although the targeted maximum increase of 1.5 °C.<sup>[1]</sup> This is due to the failure in achieving most of the targets in emission reduction for the last 7 years. This results in their ineffectiveness.

This issue has been acknowledged during the 26th Conference of the Parties (COP26) in 2021. To counteract the CO<sub>2</sub> increasing trend, more than 50 countries and the whole Europe Union pledged to halve emissions over the next decade and reach net zero emission (NZE) of carbon by 2050, aiming at limiting the global temperature rise to 1.5°. According to the NZE scenario, the electricity sector will need to supply 37 000 TWh worldwide in 2030, i.e., an increase of 40% compared to the present production. The additional installed power needs to come almost exclusively from renewable power generation that will reach an astonishing 61% share of the total electricity generated by 2030. The share of new solar PV and wind turbines must more-than-quadruple by 2030, going from the current 9% to 41%, taking advantage of their low-cost installation and policy support. A major inconvenience for the energy transition is the increased variability of both the demand and supply sides in the energy equation. Fundamentally, increasing wind and solar PV share to the abovementioned magnitude will introduce imbalances and instabilities on the power grid tied to the intermittency and unpredictability of these sources.<sup>[2]</sup> This issue is

## 1. Introduction

The energy sector—which encompasses electricity and heat generation, transportation, and industry—is responsible for almost 75% of the global CO<sub>2</sub> emissions worldwide. This is

L. Barelli, L. Trombetti  
Department of Engineering  
University of Perugia  
06125 Perugia, Italy

A. Di Michele, L. Gammaitoni  
Department of Physics and Geology  
University of Perugia  
06123 Perugia, Italy

J. Asenbauer, S. Passerini  
Helmholtz Institute Ulm (HIU)  
89081 Ulm, Germany  
E-mail: stefano.passerini@kit.edu

J. Asenbauer, S. Passerini  
Karlsruhe Institute of Technology (KIT)  
76021 Karlsruhe, Germany

 The ORCID identification number(s) for the author(s) of this article can be found under <https://doi.org/10.1002/ente.202200441>.

© 2022 The Authors. Energy Technology published by Wiley-VCH GmbH. This is an open access article under the terms of the Creative Commons Attribution License, which permits use, distribution and reproduction in any medium, provided the original work is properly cited.

DOI: 10.1002/ente.202200441

worsened by the increasing electrification of road transportation and residential heating, which will add daily and seasonal variability on the electricity demand with the potential to reshape electricity load curves and increase the intensity of the fluctuations.<sup>[3]</sup> Managing the combined effect of variable electricity supply and demand, especially over longer timeframes, without resorting to emissions-intensive fuels requires a fundamental restructuring of the energy systems. Future energy systems will not be able to rely on the flexibility provided by fossil fuels. Thus, a much more complex network of interactions, interlinking multiple sectors that supply electricity, fuels, and storage needs to be established. Energy storage will be essential to provide the system flexibility needed, meeting seasonal demand for energy as well as helping smoothing peaks in renewable power generation.<sup>[4]</sup> Such different timescales of the fluctuations require different types of response from storage, influencing what types of storage technology will best serve the system. Long-term energy storage requires carriers that offer the characteristic performance of fossil fuels—high reactivity, ease of use, transportability, and high (volumetric) energy density—both produce no CO<sub>2</sub> emissions at any point of the energy chain. So far, hydrogen has been considered the most suitable candidate.<sup>[5,6]</sup> In fact, it offers the highest gravimetric energy density of all known substances, carbon-neutrality when produced through renewables (i.e., green hydrogen), and flexibility in utilization. Whether through re-electrification by means of gas turbines and fuel cells or use in power-to-x pathways, hydrogen can supply energy to multiple applications across different sectors. According to the IEA report, the NZE scenario forecasts the total green hydrogen production to reach 5000 TWh in 2030, of which 50% will be produced via electrolysis. The second half will be generated via steam methane reforming (SMR) to be made “blue” via carbon capture and storage. This vision must contend with a much harsher reality, considering that of the total 90 Mt (3000 TWh) of hydrogen produced worldwide in 2020, less than 1% was produced through electrolysis. In addition, if all planned and announced electrolyzer projects were to be completed on time, production will reach about 278 TWh of green hydrogen, slightly more than 10% of the projected production in the NZE.<sup>[7]</sup> Moreover, issues arise also in other steps of the hydrogen value chain, e.g., a low transportation/distribution and storage efficiency (RTE) in power-to-power applications (30% by implementing low-temperature technologies and 200 bar storage<sup>[8]</sup>), and safety risks. In fact, hydrogen has a critical issue when used as a storage medium due to its very low volumetric energy density,<sup>[9]</sup> which strongly limits the ability to store and transport hydrogen and questions its viability as an energy carrier.<sup>[10]</sup> It is remarked as long-term energy storage demand is assessed in about 3000 TWh year<sup>-1</sup> at the European level to allow full decarbonization as required in 2050.<sup>[11]</sup> Considering the volumetric energy density of hydrogen compressed @700 bar (1.4 kWh L<sup>-1</sup>) or liquefied (2.3 kWh L<sup>-1</sup>), a need of about 2.1/3.6 billion cubic meters is required as net annual storage volume, with a gross volume significantly greater due to the storage plant complexity.

In this context, reactive metals are gaining increasing attention as energy carriers. The storage phase can be performed by means of well-established industrial processes, supplied with renewable electricity, already installed at the multi-MW power order for metals production. With regard to the utilization phase,

reactive metals enable both electrochemical (e.g., metal–air primary batteries) and thermodynamic pathways for their conversion. The latter, very suitable for long-term storage applications, consists of the metals’ oxidation with water or steam to provide hydrogen and heat (which can be both converted to power) and metal oxides. These can be recycled back to the metals production plants. Thus, reactive metals are an interesting option for power-to-power and power-to-x applications fully embracing the circular economy and recyclability principles needed for the transition to a net zero emissions economy.

Among the reactive metals, Al is a promising candidate due to its abundance and well-established supply chain. Al is produced via the electrolytic reduction of alumina (Al<sub>2</sub>O<sub>3</sub>) by means of the Hall–Héroult process. This reduction process requires only electricity, which produces significant carbon intensity reduction when supplied by renewable electricity.

The process consists of the electrolysis in a cell containing a bath of molten cryolite (Na<sub>3</sub>AlF<sub>6</sub>) at temperatures of 950–1000 °C in which the alumina is dissolved.<sup>[12]</sup>

In this regard, innovative technologies are considered to enable Al as energy carrier, specifically, the inert anodes and the wettable cathodes ones. These are already at the demonstration level and their full commercialization can be expected by 2030.<sup>[13]</sup>

The implementation of dimensionally stable, inert anodes allows to avoid CO<sub>2</sub> and perfluorochemicals (PFCs) emissions produced by the Hall–Héroult process.<sup>[14]</sup> Inert anodes release oxygen instead of carbon dioxide during the process, successfully eliminating greenhouse gases (GHG) emissions. Wettable cathodes, made of inert titanium diboride (TiB<sub>2</sub>), allow to reduce aluminum smelter specific consumption by 15–20% with respect to the current best practice. This is characterized by a specific energy need of 13 kWh kg<sub>Al</sub><sup>-1</sup><sup>[13]</sup> versus a theoretical energy of 6.232 kWh kg<sub>Al</sub><sup>-1</sup>.<sup>[15]</sup>

Additionally, Al is highly recyclable and is not a critical raw material. The long-term availability of bauxite global resources (from 55 billion to 75 billion tons of bauxite ores) is guaranteed and located also in politically stable countries.<sup>[16]</sup>

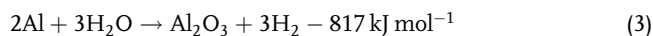
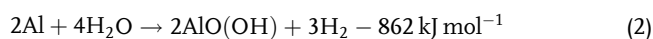
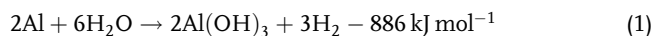
Previous works of the authors demonstrate that the use of Al as storage media and its conversion based on steam oxidation allow to reach RTE in power-to-power applications of about 36% with higher safety than H<sub>2</sub> and a volumetric energy density of 23.5 kWh L<sup>-1</sup>.<sup>[17]</sup> Thus, the net storage volume demand previously assessed is reduced of 10 and 16 times with respect to the case of liquefied H<sub>2</sub> and H<sub>2</sub>@700 bar, respectively. Moreover, also the electricity and hydrogen cogeneration is considered, resulting in a greater economic convenience with respect to electrolysis for what concerns hydrogen production. Al-based H<sub>2</sub> production cost is estimated in the range of 4.2–9.6 € kg<sup>-1</sup> H<sub>2</sub>, while wind and solar power based green H<sub>2</sub> production cost varies from 6.5 to 12.1 € kg<sup>-1</sup> H<sub>2</sub>.<sup>[18]</sup>

This study focuses on the realization of an experimental test bench to investigate aluminum oxidation with steam at temperatures up to 900 °C while varying other operational parameters, such as the steam to aluminum ratio and the gas hourly space velocity. Considering the lack of experimental results about high-temperature steam oxidation, an innovative investigation is presented providing a sensitivity analysis of Al steam oxidation in the temperature range of 600–900 °C. Also, aluminum quantity and water mass flow are varied separately. To assess the potential for energy production applications, reaction times

and hydrogen production rate and yield are in focus. Finally, the chemical analysis of the resulting powder is used to validate the results obtained in terms of parameters effect on reaction rate and to gather information for the future optimization of the reactor management.

## 2. State of the Art of Aluminum Oxidation

The reaction of aluminum and water produces hydrogen and aluminum oxide and/or hydroxide as illustrated in Equation (1)–(3)



A computational study, performed to predict the favorability of the end product,<sup>[19]</sup> reports that  $\text{Al}(\text{OH})_3$  (Gibbsite) is formed at ambient pressure below 294 K,  $\text{AlO}(\text{OH})$  (Boehmite) from 294 to 578 K, and  $\text{Al}_2\text{O}_3$  (alumina) above 578 K. Every reaction produces 0.11 kg of  $\text{H}_2$  and 15.84 MJ of thermal energy (calculated on the HHV of hydrogen) per kg of aluminum, if completed.<sup>[20]</sup>

The mechanism of aluminum oxidation by water involves the hydration of the thin aluminum oxide layer covering the aluminum particles. Following, the hydroxide ions diffuse through the surface layer to reach the underlying aluminum,<sup>[21]</sup> which is the rate-limiting step. Thus, increasing the temperature as well as the particles surface area enables higher conversion rates and shorter reaction times. The combined effect of temperature and surface area causes no reactivity for micrometer-sized aluminum particles at ambient temperature.<sup>[22]</sup> For this reason, research efforts were aimed at finding different methods to damage the integrity of the oxide layer and mitigate its formation, so that the reaction can continue until aluminum is fully oxidized and hydrogen yield is maximized. Common methods include the utilization of alkaline compounds,<sup>[23]</sup> mechanical activation,<sup>[24]</sup> and metal alloying.<sup>[25]</sup> Moreover, as micrometer-sized particles are unable to be completely oxidized in water, some researchers shifted their focus on nanometric powders,<sup>[26]</sup> achieving increased reaction rates and hydrogen yields.

The methods for aluminum activation have in common one glaring energy-related problem. With such low-temperature reactions, approximately half of the energy contained in the aluminum powder is lost as waste heat during the metal–water reaction.

Consequently, also aluminum oxidation by pressurized water at temperatures between 100 and 350 °C was investigated.<sup>[27–29]</sup> Reported conversion rates are up to 100% over a time span of minutes in batch reactors. While the results are excellent, batch operating conditions are not suitable for continuous operation of energy-conversion devices such as turbines and fuel cells. Moreover, reactions that occur at these temperatures produce either gibbsite or boehmite, both requiring more water, and therefore achieving lower energy densities, compared to the reaction that produces alumina.

More recent studies on the topic investigated innovative pathways for aluminum oxidation focused on the use of supercritical

water. The results highlight 100% hydrogen yields from coarse aluminum particles and scrap aluminum at temperatures above 647 K and pressures above 220 bar. Results also suggest that maximum reaction rates increase significantly as water density increases.<sup>[30,31]</sup>

A higher temperature oxidation between aluminum and steam is theoretically able to achieve higher power densities and Carnot efficiency compared to the reaction with water.<sup>[32]</sup> Aluminum can burn in steam producing flame temperatures above 3000 K,<sup>[33]</sup> as detailed in some papers presenting the design and test of novel aluminum–steam combustors.<sup>[34–36]</sup> Whereas the reported combustion efficiency can reach more than 95%, the management of the formation and clumping of aluminum oxide still represents the greatest challenge for a steady and lasting combustion. Moreover, only produced heat is exploited, resulting in the waste of up to half of the energy within the metal fuel.

No previous studies are available concerning oxidations by steam carried out at intermediate temperatures, specifically in the 600–900 °C temperature range. As the reaction follows the Arrhenius law, a faster oxidation compared to the reaction with water is supposed to take place, but there is no clear indication if the oxidation rate is suitable for supporting continuous operating conditions and operating parameters effect on the reaction kinetics. Moreover, no information is available in the literature about the effect of alumina clogging in this temperature range.

## 3. Experimental Section

### 3.1. Test Bench Description

The test bench layout is presented in **Figure 1**. The core component is the oxidation reactor (6), which is a small stainless-steel capsule containing the aluminum powder. The reactor is flushed with nitrogen prior to being heated at the desired temperature for the test to avoid the aluminum oxidation with air. After the temperature reaches the desired value, steam is sent to the reactor for the aluminum oxidation to occur. A mass flow controller (2) conveys a suitable water stream from the pressurized tank (1) into the vapor generator (3). As the reaction is carried out under an overstoichiometric water flow, the stream exiting the reactor is a mixture of water and hydrogen. Thus, water is first condensed in the water trap (7) to measure downstream the generated hydrogen flow through the flow meter (8).

#### 3.1.1. Water Mass Flow Controller

The deionized water employed for the tests is stored in a pressurized fiberglass cylinder pressurized at 3 bar by means of compressed air. The mass flow controller is a Quantim Coriolis from Brooks Instrumental. The maximum flow rate is  $150 \text{ g h}^{-1}$ , whereas the usual flow during tests is about  $60 \text{ g h}^{-1}$ . The achieved accuracy, in terms of measured water after 1 h of operation, is  $\pm 0.5\%$ . The mass flow controller is equipped with a suction valve pressure rated at 3 bar, but every component downstream the flow controller is just slightly pressurized to overcome the pressure drop of the circuit. The mass flow

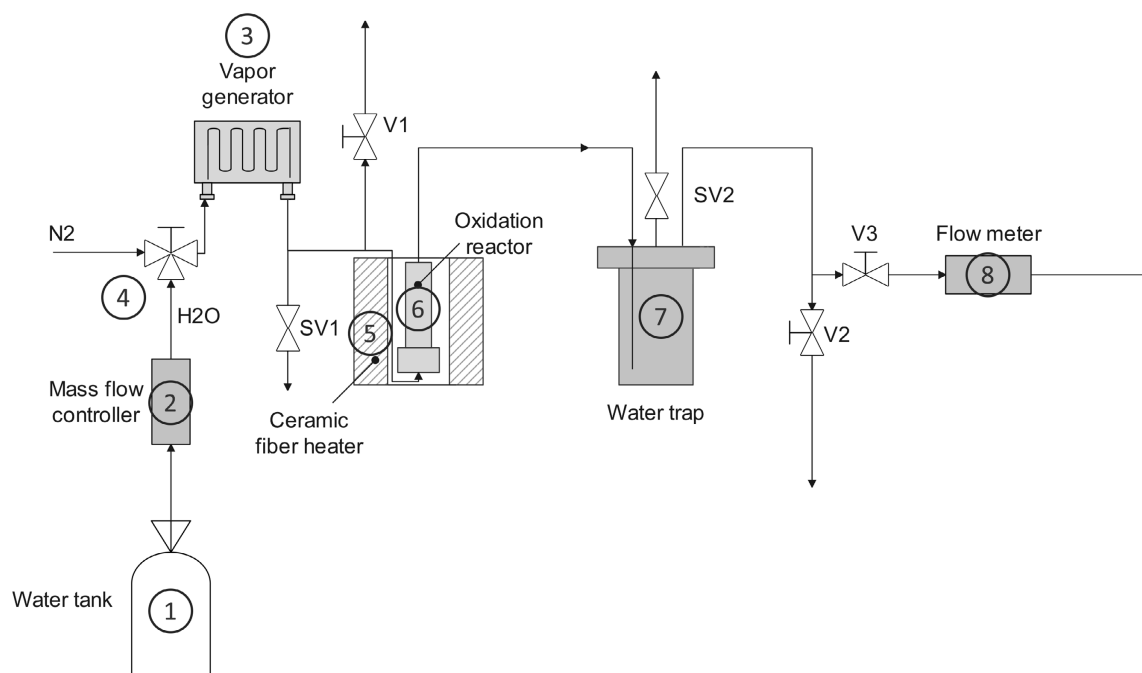


**Figure 1.** Test bench layout.

controller is operated through an external control and read-out unit allowing the user to set the desired mass flow.

### 3.1.2. Steam Generator

The steam generator is composed of two metal plates with an engraved serpentine pattern, sealed together, and placed on an electric-powered heating plate. A thermocouple inserted within the heating plates enables to fix their temperature at 240 °C to maintain a constant water vapor flow along the entire duration of the test.

As the circuit must be flushed with nitrogen before each test, a switch is inserted between the flow controller and the vapor generator. Upon nitrogen flushing-side the circuit is connected to the external pressurized nitrogen line. When switched to the water vapor side, it allows water to flow freely from the flow controller to the vaporizer acting as the control valve for the water vapor flow.

### 3.1.3. Ceramic Fiber Heater

The heating system for the oxidation reactor is composed of a ceramic fiber heater (Watlow model VC404A06A-0001R) with the shape of a hollow cylinder, rated power of 900 W AC, and maximum operating temperature of 1100 °C. A closed loop controller circuit is realized for power regulation, based on a high-temperature thermocouple and an Arduino programmable board for temperature control. The controller circuit regulates the ceramic heater's power supply, uses a leading-edge phase control dimming method to lower the output power depending on the measured temperature and the set point. The controller

also records the fiber heater and the heating plate temperatures. An aluminum vessel hosts the ceramic heater as well as the thermal isolation made with a 3 cm thick, superwool fiber layer (RS components). The vessel is covered with a circular lid.

### 3.1.4. Oxidation Reactor

The oxidation reactor is a small hollow 316 steel cylinder (14 cm length × 1 cm diameter) with a screw cap on one side and a closed end on the other. Due to the high temperatures reached by the reactor, a copper gasket is installed on the base of the cap to achieve the gas-proof sealing.

### 3.1.5. Water Trap

The water trap downstream from the reactor is used to condense the steam flowing out. It is made of stainless steel and has a volume of about 2 L, 2/3 of which is filled with deionized water prior to start the test. The incoming stream is forced to pass through the water by means of a polytetrafluoroethylene (PTFE) tube reaching the bottom of the trap. This is essential to guarantee that the steam contained in the stream condenses while passing through the trap. To assure an outlet flow of dry hydrogen, the water trap's temperature is kept below 15 °C.

### 3.1.6. H<sub>2</sub> Flow Meter

The flow meter chosen for the application is a model 5800-S from Brooks. It is calibrated on a flow of 0–5 L h<sup>-1</sup> of CO but can be used to measure a H<sub>2</sub> flow using the conversion tables provided by the manufacturer. The flow meter communicates through a RS-232 port to a PC for gas flow data recording.

### 3.2. Aluminum Powder Preparation

The powder selected for the test bench is a mesh 325 (particle diameter  $<44\ \mu\text{m}$ ) aluminum powder from Alfa Aesar. The aluminum powder is mixed with granulated perlite, serving to mitigate the aluminum powder agglomeration when the reactor is loaded and during the oxidation process. A fixed amount of perlite (0.4 g), which does not take part to the chemical reaction, is used in all tests. The various aluminum–perlite mixtures are manually mixed until the aluminum powder is well distributed on the surface of the perlite grains before loading in the reactor. To assure that no powder moves from the reactor dragged by the steam flow, small pieces cut from a superwool fiber roll are shaped in the form of cylindrical plugs and inserted in the reactor above and below the loaded powder mixture. After tightening the cap, the capsule is pressurized at 3 bar to check for gas leakage. Afterward, the reactor is connected to the test bench circuit and allocated inside the ceramic heater. The thermocouple for the Arduino controller circuit is put in contact with the capsule external surface.

### 3.3. Test Procedure

First, the circuit is flushed with nitrogen for 5 min to ensure the oxygen removal. After, valve V2 in Figure 1 is closed. Then, valve V3 is set to open and gas flow is monitored until the system is in equilibrium and the flow stops. Afterward, the fiber heater is powered while monitoring the oxidation reactor's temperature until it reaches equilibrium. The  $\text{H}_2$  flow meter is used to monitor the volume flow due to the expansion of the nitrogen inside the capsule during the temperature ramp. Further details regarding the measurement of hydrogen production at the net of the nitrogen displacement are provided in the following Section 3.3.1. At this point the test is launched by directing water to the vapor generator. During the 1 h duration of the test, the water trap's temperature is kept below  $15\ ^\circ\text{C}$ . After 1 h of test the internal valve of the flow controller is closed to stop the water flow. The hydrogen flow progressively declines reaching zero within a few minutes.

After the execution of each test the reactor is open and unloaded. A sample of the reaction products is collected. Ex situ characterization of the collected samples is performed by scanning electron microscopy-energy dispersive spectroscopy (SEM-EDS) and X-ray diffraction (XRD) measurements.

SEM images were recorded with a Zeiss Crossbeam 340 field-emission electron microscope, using a secondary electrons detector. Elemental mappings are performed with an energy dispersive X-ray (EDX) spectrometer (Oxford Instruments X-Max Xtreme,  $100\ \text{mm}^2$ , 1–5 kV).

The XRD spectra are recorded by Philips X'Pert PRO MPD diffractometer operating at 40 kV and 40 mA, with a step of  $0.03^\circ$  and a time per step of 30 s using Cu  $\text{K}\alpha$  radiation and a X'Celerator detector. Patterns are obtained by continuous scanning from  $15^\circ\ 2\theta$  to  $75^\circ\ 2\theta$ .

#### 3.3.1. Hydrogen Flow Rate Measurements Details

As mentioned before, at the start of any test the circuit is filled with nitrogen. When the water flow starts, there are three major inconveniences.

First, when water evaporates it increases its volume. This creates a local overpressure that pushes some of the nitrogen out, which would be measured as hydrogen by the flow meter (8). To address this problem, the relief valve V1 (in Figure 1) is kept open during the first minute of the test to discharge this overpressure in atmosphere, so no hydrogen gas flow is measured over the initial 60 s.

Secondly, when water vapor enters in the reactor, it pushes nitrogen out of it. Because of the small quantity of aluminum used, this amount is not negligible. Furthermore, calculating the volume of this gas is practically impossible without incurring in some serious approximation errors. Instead, it was opted to perform a set of dummy tests at the selected temperatures in the scheduled campaigns. These tests follow the same procedure explained in Section 3.2 and 3.3, but with only perlite (no aluminum) loaded in the reactor. So, for each operating temperature, the evolution of the gas flow rate displaced by water's movement to the trap is measured and integrated ( $V_{\text{in}}$  is the resulting volume) over the test duration. After the execution of each of the test reported in Table 1–3,  $V_{\text{in}}$  (the one assessed at the same temperature of the considered test) is subtracted to the overall nitrogen displacement and hydrogen production ( $V_{\text{tot}}$ ) resulting by the integration of the gas flow rate measurements at the reactor outlet during the test.

Finally, the water flow is also factored in the measure. As water vapor condenses in the trap along the test, the water level in the trap slowly rises. This reduces the gas space available in the trap and causes an additional contribution to the measured flow. To exclude this effect, the volume  $V_w$  occupied by the amount of

**Table 1.** Test campaign—below aluminum melting point.

Test ID	Temperature [ $^\circ\text{C}$ ]	Water flow [ $\text{g h}^{-1}$ ]	Al quantity [g]	$\text{H}_2$ volume [mL]	%CR
600-60-0.2P	600	60	0.2	13.43	5.44%
650-60-0.2P	650	60	0.2	12.04	4.88%
550-60-0.2P	550	60	0.2	5.7	2.31%
600-75-0.2P	600	75	0.2	8.96	3.63%
600-45-0.2P	600	45	0.2	8.36	3.39%
600-60-0.25P	600	60	0.25	11.11	3.6%
600-60-0.15P	600	60	0.15	13.97	7.55%

**Table 2.** Test campaign—above aluminum melting point.

Test ID	Temperature [°C]	Water flow [g h <sup>-1</sup> ]	Al quantity [g]	H <sub>2</sub> volume [mL]	%CR
800-60-0.2P	800	60	0.2	47.33	19.19%
850-60-0.2P	850	60	0.2	76.21	30.89%
750-60-0.2P	750	60	0.2	31.25	12.67%
800-75-0.2P	800	75	0.2	36.76	14.90%
800-45-0.2P	800	45	0.2	48.98	19.86%
800-60-0.25P	800	60	0.25	38.95	12.63%
800-60-0.15P	800	60	0.15	30.81	16.66%

**Table 3.** Test campaign—900 °C.

Test ID	Temperature [°C]	Water flow [g h <sup>-1</sup> ]	Al quantity [g]	H <sub>2</sub> volume [mL]	%CR
900-60-0.2P	900	60	0.2	175.46	71.13%
900-75-0.2P	900	75	0.2	135.39	54.89%
900-45-0.2P	900	45	0.2	180.39	73.13%
900-60-0.25P	900	60	0.25	198.37	64.34%
900-60-0.15P	900	60	0.15	113.15	61.13%

water used during the test is subtracted to the measured hydrogen production, considering the volume of reacted water negligible (three orders of magnitude lower) compared to the one supplied to the circuit.

### 3.4. Test Campaigns

Two different test campaigns were performed dealing with aluminum below (i.e., 550–650 °C, see Table 1) and above (i.e., 750–850 °C, see Table 2) its melting point.

Each campaign was designed to evaluate the effect of either operating temperature, aluminum quantity, or water flow rate on the hydrogen production rate and total yield. Accordingly, Table 1 illustrates the explored combinations of temperature (from 550 to 650 °C) Al quantity (from 0.15 to 0.25 g) and water flow (45–75 g h<sup>-1</sup>). These same combinations are shown in Table 2, except for the temperature, which ranges from 750 to 850 °C.

All tests listed in Table 1 and 2 were performed within 1 h regardless of the flow measured at the end. After 1 h water feeding was interrupted, while hydrogen flow was measured and integrated until it reached zero.

A third test campaign was performed at 900 °C. Tests details are summarized Table 3. The duration of the tests was also fixed at 1 h as for the previous campaigns. Data relative to the obtained hydrogen volume and aluminum conversion rate (%CR) reported in Table 1–3 are presented and discussed in the following Section 4.

## 4. Results

The hydrogen total volume ( $V_{H_2}$ ) is calculated by integrating the measured flow rate (8) over the test (obtaining  $V_{tot}$ ), i.e., until the flow hits zero, and subtracting the volume of nitrogen  $V_{in}$

at the beginning of the test and of the water ( $V_w$ ) used during the test (see details in Section 3.3.1.).

Measured volume at standard conditions (273.15 K, 1 atm), converted to produced hydrogen mass as in Equation (4), allows to assess the mass of reacted Al ( $m_{Al,R}$ ) as indicated in Equation (5). Full aluminum conversion yields to 11.1% of the aluminum mass converted into hydrogen. Finally, Equation (6) provides the aluminum conversion rate (%CR) as the ratio of reacted ( $m_{Al,R}$ ) and loaded ( $m_{Al,L}$ ) aluminum masses.

$$m_{H_2} = V_{H_2} * \rho_{H_2, standard} \quad (4)$$

$$m_{Al,R} = \frac{m_{H_2}}{0.111} \quad (5)$$

$$\%CR = \frac{m_{Al,R}}{m_{Al,L}} \quad (6)$$

As evident in Table 1, at temperature below the aluminum melting point the conversion rate is quite low and hardly sensible to changes in water flow, aluminum amount, and temperature. Only a little increase in performance when reducing the powder content is highlighted.

The summary results of the test campaign at 800 °C, above aluminum melting point, are reported in Table 2. Aluminum conversion rate values are significantly higher than those obtained in the previous test campaign. The operating parameters affect %CR, mainly, the temperature increase positively impacts hydrogen production, indicating that melting aluminum is an important factor for the reaction kinetics.

Temperatures around 800 °C are relevant on both the short-term (Figure 2a) and long-term (Figure 2b) hydrogen production. After less than 1 min, hydrogen production rises steadily reaching increasingly higher values with higher temperatures. It is

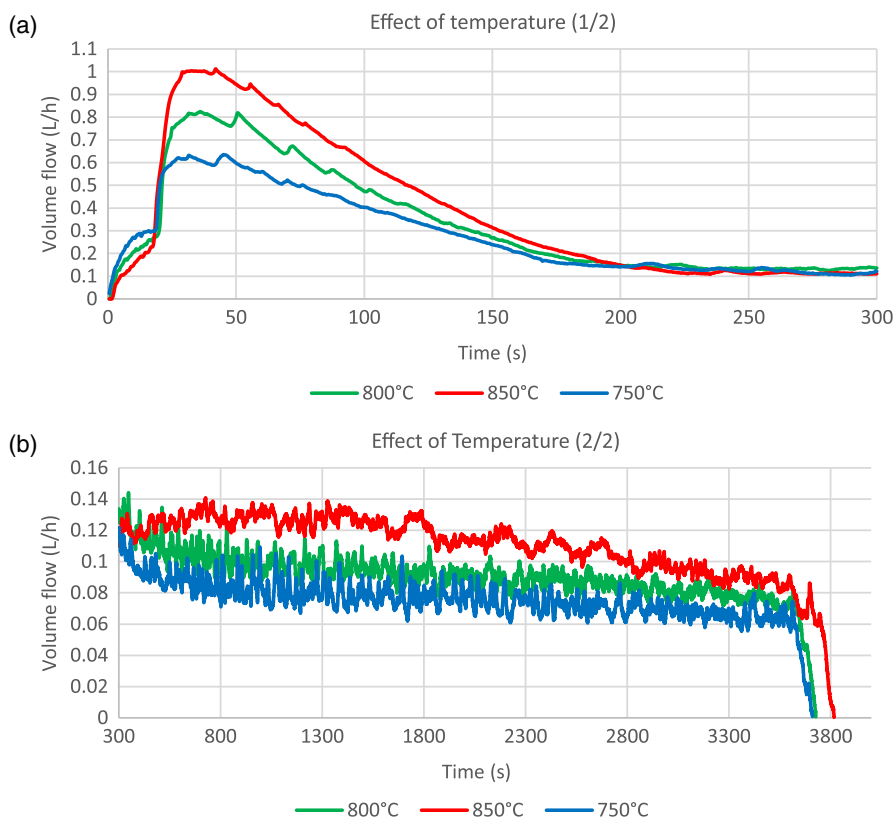


**Figure 2.** Temperature effect on hydrogen production: a) initial 300 s—the smaller peak in the first 20 s is due to the nitrogen displacement pushed by the steam flow; b) from 300 s to the end of the test.

highlighted as the bulk of the recorded flow is due to the water displacement effect discussed above.

The results of test campaign above the aluminum melting point suggested for an exploration at an even higher temperature, specifically 900 °C. Details are presented and discussed in Section 4.1.

It must be highlighted that all tests performed followed a two-stage reaction behavior, with a first stage characterized by a hydrogen production peak occurring within the first minute after closing the relief valve V1 being followed by a second stage characterized by low hydrogen release rate, which takes up almost the entire duration of the 1 h test. This two-stage behavior is associated to the high reactivity of the powder, readily reacting with the incoming steam. However, the reaction results into the formation of a thin oxide layer drastically slowing the reaction rate. Nonetheless, the reaction occurs for the whole duration of the test.

#### 4.1. Test Campaign at 900 °C

The obtained results, summarized in Table 3, highlight remarkable aluminum conversion rates up to about 73%.

##### 4.1.1. Effect of Water Flow

As pictured in Figure 3, the water flow seems to have a very distinctive effect on hydrogen production behavior. The

hydrogen production on the short term (Figure 3a) and long term (Figure 3b) increases by reducing the water flow, as already indicated by the overall H<sub>2</sub> production and aluminum %CR data in Table 3. It is highlighted that the hydrogen production peak occurs earlier when using higher water flows because the steam reaches earlier the reactor.

##### 4.1.2. Effect of Aluminum Quantity

As depicted in Figure 4, the behavior of the reaction strongly differs as the quantity of aluminum loaded is modified. The reduction of the loaded aluminum quantity results in delaying the hydrogen production and, obviously, lowering the overall hydrogen production. Moreover, the reaction kinetics is significantly improved because about half of the hydrogen production occurs in the first 300 s of the test. However, the aluminum %CR decreases with the loading going from 0.25 to 0.2 g to increase again for a reduction to 0.15 g.

#### 4.2. Analysis of the Reaction Products

Ex situ characterization of the reaction products was performed only for the most representative tests, specifically 600-60-0.2P, 750-60-0.2P, 800-60-0.2P, 850-60-0.2P, and 900-60-0.2P.

For all these tests, water flow rate and loaded aluminum are set at 60 g h<sup>-1</sup> and 0.2 g, respectively, while temperature

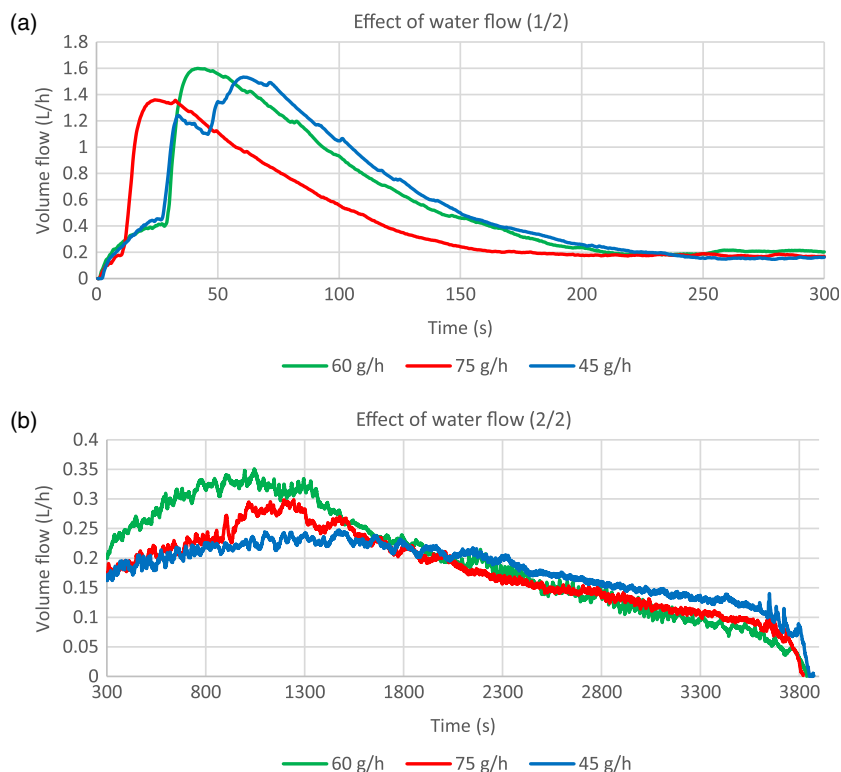


**Figure 3.** Water flow rate effect at 900 °C: a) initial 300 s—the smaller peak in the first 20 s is due to the nitrogen displacement pushed by the steam flow; b) from 300 s to the end of the test.

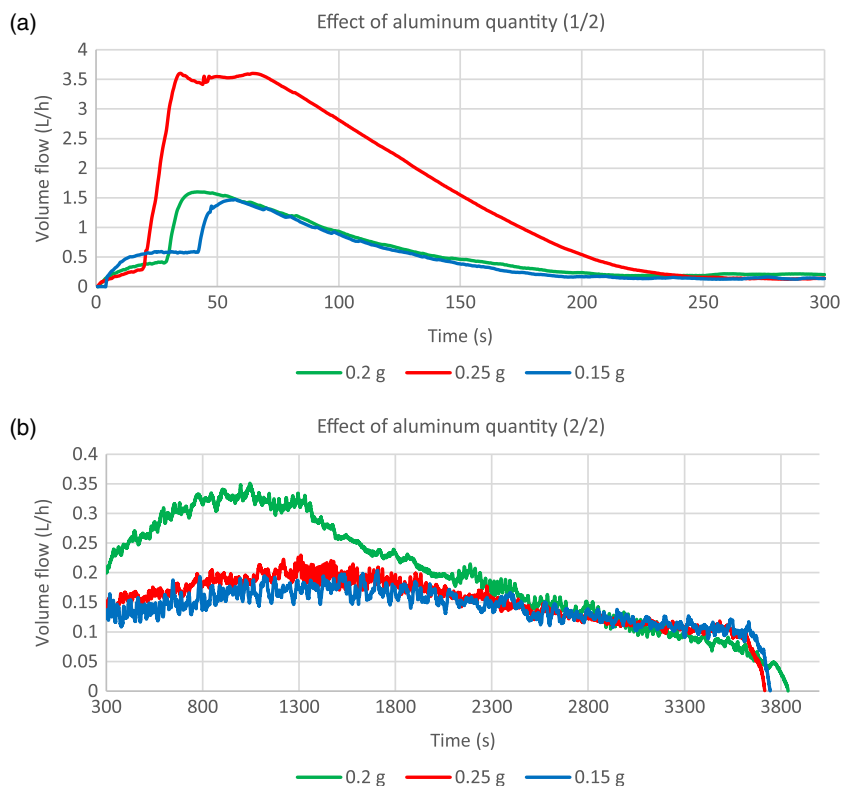


**Figure 4.** Aluminum quantity effect at 900 °C: a) initial 300 s—the smaller peak in the first 20 s is due to the nitrogen displacement pushed by the steam flow; b) from 300 s to the end of the test.

varies from 600 to 900 °C. The analysis allows to highlight structural and chemical modifications varying the temperature, being the parameter that most affects aluminum conversion rate.

#### 4.2.1. Morphological Analyses

**Figure 5** depicts SEM images taken from the reaction products of the tests specified above.

For all five samples, SEM images were recorded to investigate the surface of the particles and their general morphology. Furthermore, EDX mapping was used to track the degree of aluminum's oxidation. For this purpose, the mapping of aluminum, silicon (from perlite and glass wool) and oxygen are shown in Figure 5. As the oxygen content in SiO<sub>2</sub> (from inert glass wool and perlite) does not change upon reaction, it can be used as a reference for the quantitative determination of aluminum's oxidation. The images show that at 600 °C (Figure 5a) the surface of

the spherical aluminum microparticle is smooth and intact and shows no signs of exfoliation. Also, the EDX mapping shows a very weak oxygen signal for the Al particles, indicating the presence of only a thin alumina layer and no bulk oxidation. For the sample at 750 °C, the surface still looks generally smooth, but a close look reveals that very few flake-like particles are formed on the surface. Yet, the overall oxygen content in the oxygen mapping is still low. Starting from 800 °C the surface of the aluminum's particles looks drastically different. As shown in Figure 5c, the whole surface of most particles is covered by defoliated microparticles. Also, the strong oxygen signal in the EDX shows that at least the surface of most particles is completely oxidized. Yet, some particles in the sample still show a rather smooth surface, indicating that the conversion yield of the process is still low. Eventually, the surfaces of the particles in the 850 and 900 °C samples (Figure 5d,e) are completely covered in small flake-like and spherical particles and show a strong signal in

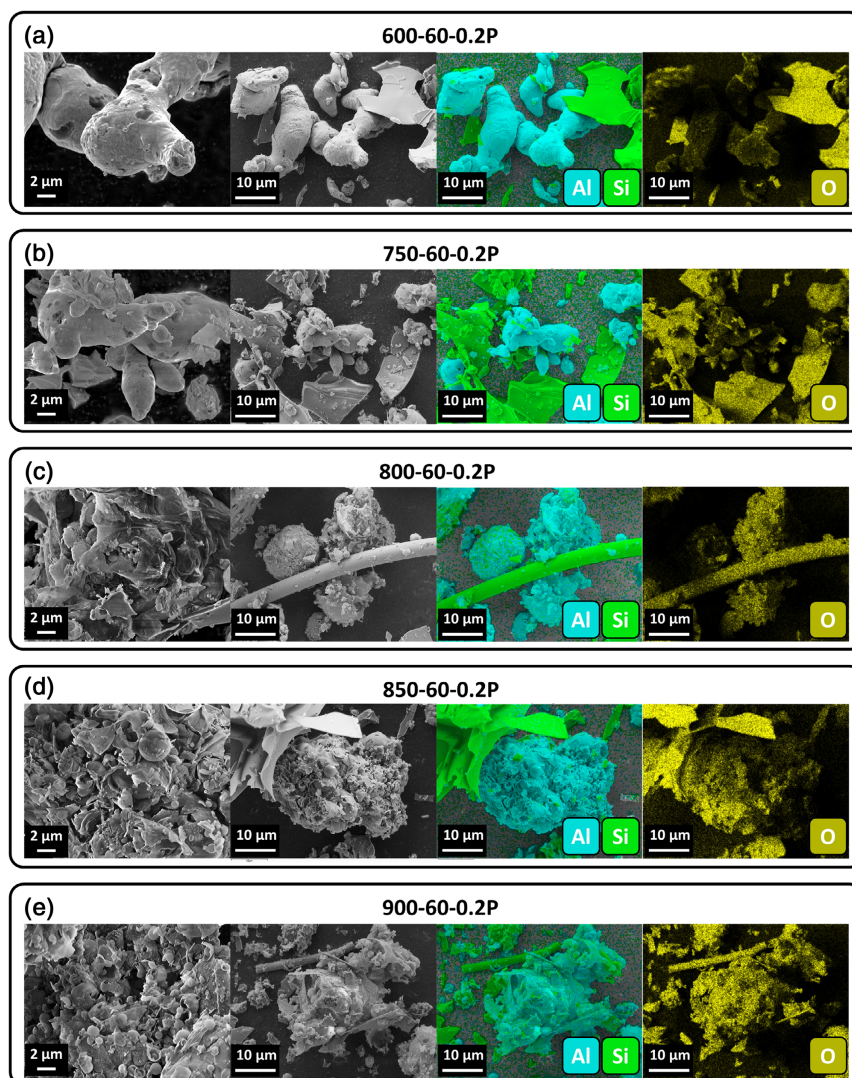


**Figure 5.** SEM-EDX images of the reaction products as collected after tests of a) 600-60-0.2P; b) 750-60-0.2P; c) 800-60-0.2P; d) 850-60-0.2P; and e) 900-60-0.2P. From the left to right the first two columns show SEM images, recorded with a secondary electron detector, of the powders at different magnifications and the second two columns show EDX mapping of aluminum (in blue) and silicon (in green), and oxygen (in yellow), respectively.

the oxygen mapping, suggesting that the whole material is oxidized to  $\text{Al}_2\text{O}_3$ . Note that both SEM imaging and EDX mapping are surface-sensitive techniques. Thus, to investigate the degree of oxidation of the Al particles in the bulk, XRD analysis was used in the next step.

#### 4.2.2. XRD Analyses

The XRD spectra of the powder samples are illustrated in **Figure 6**.

The XRD spectrum of the reaction product at 600 °C features only the aluminum phase (JCPDS 01-085-1327) as evidenced by the characteristic peaks at 38.4°, 44.7°, and 65.1°, corresponding to the Al(1 1 1), Al(2 0 0), and Al(2,2,0) planes, respectively.

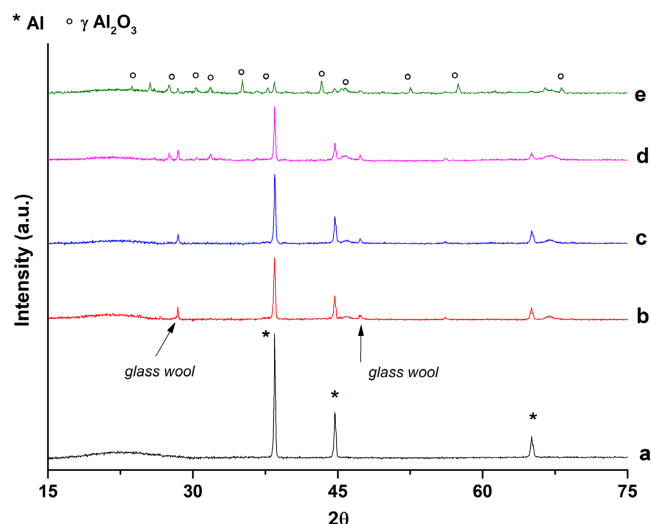


**Figure 6.** XRD spectra of the reaction products collected after the a) 600-60-0.2P; b) 750-60-0.2P; c) 800-60-0.2P; d) 850-60-0.2P; and e) 900-60-0.2P tests. The symbols \* and ° mark the characteristic Al and  $\gamma\text{-Al}_2\text{O}_3$  peaks, respectively. Features arising from glass wool particles are also indicated.

At higher temperatures, see spectra *b*, *c*, and *d*, some weak features associated to  $\gamma\text{-Al}_2\text{O}_3$  are observed, which become dominant in *e* (reaction product at 900 °C), indicating that this is the main phase. In all spectra, the amorphous peak due to pearlite (23°), the peaks due to glass wool (28° and 47°), and the peaks of unreacted aluminum are also observed.

Rietveld refinement has been used to evaluate reaction yield from the XRD pattern of the reaction product of test 900-60-0.2P. The percentage of  $\gamma\text{-Al}_2\text{O}_3$  resulted to be 83.4% while Al was 16.6%. This result confirms the very high yield aluminum conversion reaction (over 71%) evaluated via the produced hydrogen measurements. It should be noted that residual submicrometer-sized aluminum clusters, not revealed by XRD, would explain the difference in conversion yields obtained through the two measurements.

As evidenced by the abovementioned experimental test campaign, temperature plays the most important role in the reaction kinetic, increasing both initial and total hydrogen productions. This is highlighted in **Figure 7**, which depicts the aluminum conversion rate after 1 h test and the average hydrogen flow rate in the first 60 and 300 s as a function of temperature, keeping constant the quantity of aluminum loaded in the reactor as well as the water flow.

The results in **Figure 7** show that once the reaction is performed above the aluminum melting point (660 °C), an exponential correlation between aluminum conversion rate and temperature is achieved.

As described in Section 3.3, the tests end after 1 h even if hydrogen is still produced. This is an occurrence for most of the tests performed at 900 °C. Thereby making a direct measure of overall hydrogen production and aluminum conversion rate is impossible. For these tests, an estimation of hydrogen production and aluminum conversion rate could be deducted using a trend line calculated on a significant interval time of the test. The test duration is extended until the hydrogen volume flow trend equals the input water flow, signifying that hydrogen production has ended. Then, hydrogen flow is integrated, and aluminum conversion rate is calculated. With regard to the most

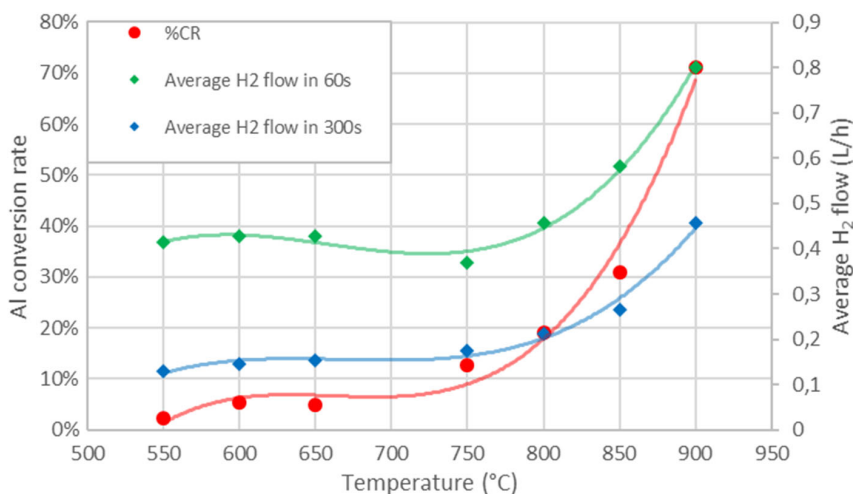


**Figure 7.** Aluminum conversion rate and the average hydrogen flow rate in the first 60 and 300 s versus temperature. Water flow rate and loaded aluminum were set at 60 g h<sup>-1</sup> and 0.2 g, respectively, for all tests.

promising test performed at 900 °C (test 900-45-0.2P), this approach results in 75% aluminum conversion rate after 75 min versus the 73.13% measured during 1 h test.

Concerning the aggregation of the aluminum particles and alumina, i.e., the clogging effect, during the conversion process, the use of perlite enables steam flowing through the oxidation reactor for the whole test duration. However, in all tests below 900 °C, alumina clogging occurs, inducing a strong adhesion of the reaction product to the inner walls of the reactor. This requires mechanical fracturing to remove the reaction product, which is clearly unfeasible in large-scale reactors. On the other hand, the tests at 900 °C reveal the formation of spherical micro-particles of alumina, which do not clog the reactor and enable the operation of a suitable reactor for the continuous steam oxidation of aluminum.

## 5. Conclusions

The present study covers the examination of aluminum oxidation with water steam using an experimental test bench. The aim is to assess the hydrogen production rate and yield, varying aluminum quantity and water mass flow at temperatures much lower than the one required for a full-fledged combustion. The results of the sensitivity analysis show that temperature has the greatest effect (exponential correlation) among the mentioned parameters, achieving a conversion rate of aluminum, assessed based on measured hydrogen production, of 73.13% at 900 °C. Water mass flow rate exhibits a slightly positive effect on the conversion rate while being reduced, but a negative impact when increased, highlighting the importance of optimizing the gas hourly space velocity. Worthy of mention is the strong reaction observed in the first minutes for the test sample at 900 °C with maximum aluminum quantity, therefore under a higher reaction kinetics. For what concerns the gathered information about a future design of an aluminum combustor it seems that oxidations at 900 °C and ambient pressure are comparable, in terms of reaction times, with results reported in the literature for water oxidation in batch pressurized reactors (up to 40 bar). Moreover, oxidations carried out at between 750 and 900 °C are characterized by the production of spherical oxidized microparticles, prevalent at the highest investigated temperature. This phenomenon, supported by the addition of inert perlite, causes the formation of alumina before particles have too much time to clump up, allowing reactor operating times up to 1 h without incurring in the clogging effect of alumina. The obtained results are promising for the continuous operating condition of a future full-scale reactor, potentially addressing the issues typical of vortex combustors using aluminum–steam combustion.

Future planned developments for the test bench concern the extension of the range of investigation on the process parameters through the upscale of the setup, including a sensitivity analysis on the aluminum particle size.

## Acknowledgements

L.B. and L.T. contributed equally to this work. The authors acknowledge the support of the European Commission under the project STORIES

(GAP-101036910). S.P. acknowledges the basic funding from the Helmholtz Association.

Open Access funding enabled and organized by Projekt DEAL.

## Conflict of Interest

The authors declare no conflict of interest.

## Data Availability Statement

The data that support the findings of this study are available on request from the corresponding author. The data are not publicly available due to privacy or ethical restrictions.

## Keywords

aluminum, green energy carrier, hydrogen production, steam oxidation

Received: April 29, 2022

Revised: July 7, 2022

Published online:

- [1] Unfccc, *Adoption of the Paris Agreement - Paris Agreement Text English*, the United Nation Council **2015**.
- [2] P. Choksi, D. Singh, J. Singh, H. C. Bloomfield, D. J. Brayshaw, L. C. Shaffrey, P. J. Coker, H. E. Thornton, *Environ. Res. Lett.* **2016**, *11*, 124025.
- [3] B. J. van Ruijven, E. de Cian, I. S. Wing, *Nat. Commun.* **2019**, *10*, <https://doi.org/10.1038/s41467-019-10399-3>.
- [4] M. Olczak, A. Piebalgs, *FSR Energy* **2018**, <https://doi.org/10.2870/35692>.
- [5] H. Blanco, W. Nijs, J. Ruf, A. Faaij, *Appl. Energy* **2018**, *232*, 617.
- [6] H. Jiang, A. P. Kulkarni, B. Rego De Vasconcelos, J.-M. Lavoie, *Front. Chem.* **2019**, *1*, 392.
- [7] IEA (2021), *World Energy Outlook 2021*, IEA, Paris **2022**.
- [8] M. A. Pellow, C. J. M. Emmott, C. J. Barnhart, S. M. Benson, *Energy Environ. Sci.* **2015**, *8*, 1938.
- [9] G. Zhao, A. S. Pedersen, *Procedia CIRP* **2018**, *69*, 529.
- [10] M. A. Rosen, S. Koohi-Fayegh, *Energy Ecol. Environ.* **2016**, *1*, 10.
- [11] A. LUT, M. Ram, D. Bogdanov, A. Aghahosseini, A. Gulagi, S. A. Oyewo, M. Child, U. Caldera, K. Sadovskaia, J. Farfan, L. S. N. S. Barbosa, M. Fasihi, S. Khalili, C. Breyer, EWG, H.-J. Fell, T. Traber, F. de Caluwe, G. Gruber, B. Dalheimer, B. Lsns, D. F. Caluwe, F. H.-J., **2019**, <https://doi.org/10.13140/RG.2.2.10143.00160>.
- [12] P. Mandin, R. Wüthrich, H. Roustan, *ECS Trans.* **2009**, *19*, 1.
- [13] S. Slingerland, M. Gancheva, A. Visschedijk, A. Boulamati, K. Rademaekers, J. Moya, R. Veen, J. Kuenen, *Energy Efficiency and GHG Emissions: Prospective Scenarios for the Aluminium Industry*, **2015**, <https://doi.org/doi/10.2790/263787>.
- [14] D. Brough, H. Jouhara, *Int. J. Thermofluids* **2020**, *1–2*, 100007.
- [15] M. Obaidat, A. Al-Ghandoor, P. Phelan, R. Villalobos, A. Alkhalidi, *Sustainability* **2018**, *10*, 1216.
- [16] U.S. Geological Survey, *Mineral Commodity Summaries*, the USGS (United States Geological Survey), **2021**.
- [17] L. Barelli, M. Baumann, G. Bidini, P. A. Ottaviano, R. V. Schneider, S. Passerini, L. Trombetti, *Energy Technol.* **2020**, *8*, 2000233.
- [18] H. Ersoy, M. Baumann, L. Barelli, A. Ottaviano, L. Trombetti, M. Weil, S. Passerini, *Adv. Mater. Technol.* **2022**, 2101400.

- [19] P. Godart, J. Fischman, K. Seto, D. Hart, *Int. J. Hydrogen Energy* **2019**, *44*, 11448.
- [20] S. Elitzur, V. Rosenband, A. Gany, *Int. J. Hydrogen Energy* **2014**, *39*, 6328.
- [21] Z. Y. Deng, J. M. F. Ferreira, Y. Tanaka, J. Ye, *J. Am. Ceram. Soc.* **2007**, *90*, 1521.
- [22] J. M. Bergthorson, *Prog. Energy Combust. Sci.* **2018**, *68*, 169.
- [23] G. N. Ambaryan, M. S. Vlaskin, A. O. Dudoladov, E. A. Meshkov, A. Z. Zhuk, E. I. Shkolnikov, *Int. J. Hydrogen Energy* **2016**, *41*, 17216.
- [24] S. S. Razavi-Tousi, J. A. Szpunar, *Int. J. Hydrogen Energy* **2013**, *38*, 795.
- [25] J. T. Ziebarth, J. M. Woodall, R. A. Kramer, G. Choi, *Int. J. Hydrogen Energy* **2011**, *36*, 5271.
- [26] G. A. Risha, S. F. Son, R. A. Yetter, V. Yang, B. C. Tappan, *Proc. Combust. Inst.* **2007**, *31*, 2029.
- [27] A. V. Bersh, A. V. Lisitsyn, A. I. Sorokovikov, M. S. Vlaskin, Yu. A. Mazalov, E. I. Shkolnikov, *High Temp.* **2010**, *48*, 866.
- [28] M. S. Vlaskin, E. I. Shkolnikov, A. V. Lisitsyn, A. V. Bersh, A. Z. Zhuk, *Int. J. Hydrogen Energy* **2010**, *35*, 1888.
- [29] M. S. Vlaskin, E. I. Shkolnikov, A. V. Lisitsyn, A. V. Bersh, *Therm. Eng.* **2010**, *57*, 794.
- [30] K. A. Trowell, S. Goroshin, D. L. Frost, J. M. Bergthorson, *Sustainable Energy Fuels* **2020**, *4*, 5628.
- [31] K. Trowell, S. Goroshin, D. Frost, J. Bergthorson, *RSC Adv.* **2022**, *12*, 12335.
- [32] J. M. Bergthorson, Y. Yavor, J. Palecka, W. Georges, M. Soo, J. Vickery, S. Goroshin, D. L. Frost, A. J. Higgins, *Appl. Energy* **2017**, *186*, 13.
- [33] J. Foote, B. Thompson, J. Lineberry, Combustion of Aluminum with Steam for Underwater Propulsion. *Advances in Chemical Propulsion* **2010**.
- [34] T. F. Miller, J. L. Walter, D. H. Kiely, in *Proc. of the IEEE Symp. on Autonomous Underwater Vehicle Technology*, IEEE, Piscataway, NJ **2002**.
- [35] X. Chen, Z. Xia, L. Huang, L. Ma, *Energies* **2016**, *9*, 1072.
- [36] X. Chen, Z. Xia, L. Huang, X. Na, J. Hu, *Energy Fuels* **2018**, *32*, 2458.